Pergamon

Geochimica et Cosmochimica Acta, Vol. 67, No. 9, pp. 1623–1634, 2003

0016-7037/03 $30.00 + .00

doi:10.1016/S0016-7037(02)01177-8

Variation in calcite dissolution rates:A fundamental problem?

ROLF S. ARVIDSON,[1,*] INCI EVREN ERTAN,[1] JAMES E. AMONETTE,[2] and ANDREAS LUTTGE[1]

[1]Department of Earth Science, MS-126, Rice University, P.O. Box 1892, Houston, TX 77251-1892, USA
[2]Environmental Molecular Sciences Laboratory, Pacific Northwest National Laboratory, Richland, WA 99352, USA

(*Received May* 17, 2001; *accepted in revised form September* 3, 2002)

Abstract—A comparison of published calcite dissolution rates measured far from equilibrium at a pH of ~ 6 and above shows well over an order of magnitude in variation. Recently published AFM step velocities extend this range further still. In an effort to understand the source of this variation, and to provide additional constraint from a new analytical approach, we have measured dissolution rates by vertical scanning interferometry. In areas of the calcite cleavage surface dominated by etch pits, our measured dissolution rate is $10^{-10.95}$ mol/cm^2/s (PCO_2 $10^{-3.41}$ atm, pH 8.82), 5 to ~100 times slower than published rates derived from bulk powder experiments, although similar to rates derived from AFM step velocities. On cleavage surfaces free of local etch pit development, dissolution is limited by a slow, "global" rate ($10^{-11.68}$ mol/cm^2/s). Although these differences confirm the importance of etch pit (defect) distribution as a controlling mechanism in calcite dissolution, they also suggest that "bulk" calcite dissolution rates observed in powder experiments may derive substantial enhancement from grain boundaries having high step and kink density. We also observed significant rate inhibition by introduction of dissolved manganese. At 2.0 μM Mn, the rate diminished to $10^{-12.4}$ mol/cm^2/s, and the well formed rhombic etch pits that characterized dissolution in pure solution were absent. These results are in good agreement with the pattern of manganese inhibition in published AFM step velocities, assuming a step density on smooth terraces of ~9 μm^{-1}. *Copyright © 2003 Elsevier Science Ltd*

1. INTRODUCTION

The dissolution of carbonate minerals has received considerable study in the geochemical kinetics literature, and calcite has been paid the most scrutiny by far (reviews are available in Sjöberg 1978; Plummer et al., 1979; Morse 1983; Morse and Arvidson 2002). Despite the accumulation of a large dataset over the past three decades, there is significant uncertainty in the absolute value of the dissolution rate under given conditions. This dataset is summarized in Figure 1 (Plummer et al., 1978; Sjöberg 1978; Rickard and Sjöberg 1983; Busenberg and Plummer 1986; Chou et al., 1989; Schott et al., 1989; MacInnis and Brantley 1992; Dove and Platt 1996; Shiraki et al., 2000). With increasing pH under alkaline conditions far from equilibrium (high undersaturation), calcite dissolution is controlled by *surface-reaction* (as opposed to transport) kinetics (Sjöberg 1976; Rickard and Sjöberg 1983). Figure 1 shows that although the data exhibit internal consistency within results from a given laboratory, absolute rates at high pH vary by well over an order of magnitude. Although this variation is less than that found in other carbonates (e.g., dolomite—Busenberg and Plummer 1982; Chou et al., 1989; Gautelier et al., 1999), it is surprising given the large quantity of experimental data available. Some of the differences in rate reflect differences in experimental conditions (e.g., ionic strength, PCO_2, alkalinity). However, it is difficult to evaluate what additional sensitivity may be present as a function of experimental and analytical methodology (e.g., steady state rates measured in flow cells versus initial rates obtained from free drift runs; geometric versus BET surface area measurements), starting materials (preparation of powders versus rotating disks, grain size, impurities, defect density), or other factors.

We are not merely concerned here with a trivial quest for the "best number," or even simply the true value. Ultimately, detailed mechanistic information pursued in current AFM work must be integrated with this kinetic dataset. If we cannot understand the origin of differences in rates derived from changes in solution chemistry, then neither can we fully understand the relationship of those rates with ones derived from AFM step velocities. Comparisons of AFM rates with the above "powder" rates point to significant additional discrepancies (Dove and Platt 1996; Shiraki et al., 2000), and major attention has been focused on the concepts of reactive surface area, roughness, dislocation density, and heterogeneity (e.g., Schott et al., 1989; MacInnis and Brantley 1992; Brantley et al., 1999; Brantley and Mellott 2000; Gautier et al., 2001).

It is our ultimate aim to understand the relationship between processes observed at the atomic scale and their bulk, phenomenological expression. In a previous paper (Luttge et al., 2003), detailed observations and dissolution rate data for dolomite collected by vertical scanning (phase shift) interferometry (VSI) were used to establish a conceptual model of the relationship between etch pit distributions and the overall dissolution rate. These data also served as the basis for a fundamental rate law (Lasaga and Luttge 2001) that provides a basic, quantitative framework for understanding the relationship between crystal dissolution mechanism and free energy. At the centerpiece of this model is the concept that dissolution in minerals is coordinated as a train of steps (*stepwaves*) propagating from etch pits formed from dislocation defects. The velocity and spacing of stepwaves share a basic functional dependency on the degree of undersaturation (ΔG). This functional dependency reproduces the basic behavior of dissolution rate as a

* Author to whom correspondence should be addressed (rsa4046@ruf.rice.edu).

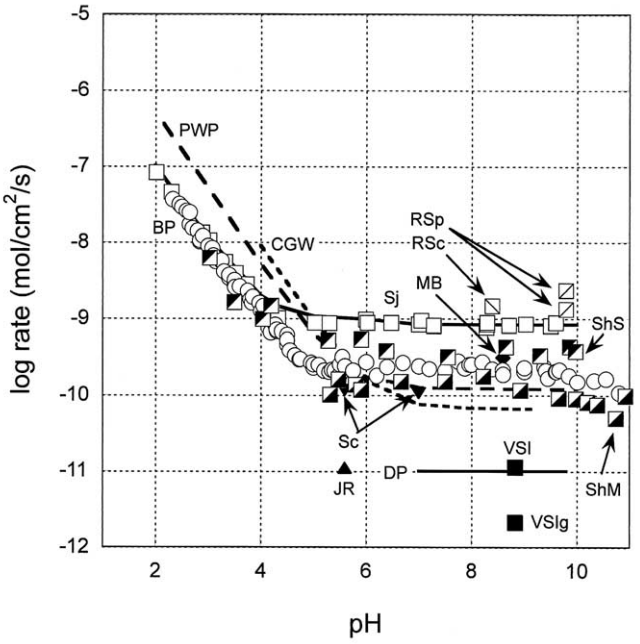

Fig. 1. Published rates of calcite dissolution. Solid line with open squares ('Sj') = Sjöberg (1978); open squares with forward slash ('RSp') = powder dissolution rates in 0.7 mol/L and 0.1 mol/L KCl media extrapolated to $\{\sqrt{Ca^{+2}CO_3^{-2}} = 0\}$, Figure 3, p. 823, Rickard and Sjöberg (1983); open square with backward slash ('RSc') = rotating disk dissolution rate in 0.7 mol/L KCl, extrapolated to $\omega = \infty$, Figure 5, p. 825, Rickard and Sjöberg (1983); coarsely dashed line ('PWP') with no symbols = Eqn. 6, p. 192, Plummer et al. (1978), assuming $[Ca^{+2}] \sim 0$; finely dashed line ('CGW') with no symbols = Eqn. 4, p. 270, Chou et al. (1989); open circles ('BP'), Busenberg and Plummer (1986); filled diamond ('MB') = 0.7 mol/L KCl-KOH solution, $PCO_2 \sim 0$, rotating unstrained cleavage surface MacInnis and Brantley (1992); inverted filled triangle ('Sc') = Schott et al. (1989); open square with filled lower right diagonal ('ShM') = AFM-derived rate, open square with filled upper right diagonal ('ShS') = rate derived from solution chemistry, both from Shiraki et al. (2000; note that DIC concentrations were 1.3 μM); Solid line with no symbol = Dove and Platt (1996); filled triangle ('JR') = rate computed from data of Jordan and Rammensee (1998; T = 24°C, $PCO_2 \sim 10^{-3.5}$) assuming a step density of 9 μm^{-1}; solid square ('VSI') = VSI datum, solid square ('VSIg') = "global" rate (this paper; rates are also tabulated in Table 1).

function of ΔG, including the observed increase in rate as sufficient undersaturation (ΔG_{crit}) is reached to allow etch pits to nucleate from hollow cores (Brantley et al., 1986; Blum and Lasaga 1987). The effect of this dissolution process is a layer-by-layer removal (consistent with AFM observations, e.g., see Liang et al., 1996) that leads to net (surface-normal) retreat of the entire surface, a result verified both by Monte Carlo simulations and dissolution experiments (Blum and Lasaga 1987; Luttge et al., 2003).

This current paper reports and discusses VSI data collected from calcite dissolution experiments in dilute $NaHCO_3$-Na_2CO_3 solutions far from equilibrium. These data also include the introduction of dissolved manganese as an inhibitor, and are linked to detailed AFM observations of dissolution under identical conditions (Lea et al., 2001). We shall show that the VSI surface-normal dissolution rate for calcite is significantly slower than the bulk rate derived from solution chemistry measured in experiments using powders or single crystals (rotating disks), consistent with the relationship observed for dolomite (Luttge et al., 2003).

2. METHODS

We measured calcite dissolution rate by time-lapse changes in mineral surface topography, mapped by VSI. An improved VSI system was used here (MicroXAM MP-8, ADE Phase Shift), offering higher resolution, an infinity-corrected optics system, larger scan range, improved light source, and enhanced analytical and data reduction software. This instrument and the basic approach have been previously described in detail (Luttge et al., 1999; 2003). VSI can quantitatively map mineral surface topography at subnanometer-scale vertical and micrometer-scale lateral resolutions, with a total field of view (10× objective) of ~ 0.5 mm^2. Image data collected at high resolution can also be digitally grafted to produce large surface mosaics. This instrument thus occupies a unique niche in its ability to integrate observations over large areas of the mineral surface, resolving not only the rates and mechanistic details of surface reactions but their spatial distribution as well. VSI observations clearly complement those made using atomic scale instruments (AFM) and bulk solution chemistry.

Interferometry measures relative surface height. By maintenance of a reference (unreacted) surface on the mineral itself, this measurement becomes absolute (Luttge et al., 1999; Beig et al., 2002). The lateral (x, y) resolution of this height measurement is a function of the objective magnification, CCD camera pixel size, and the wavelength of the reflected light; these instrument parameters are matched to provide optimal resolution. It is important to note that although each camera pixel records a single, discrete height (h_{ij}), this value accurately reflects the *mean* height of the actual mineral surface (Fig. 2B) over the area of a single pixel (Fig. 2A, 2C). At 50× magnification, the objective used for all height measurements, the lateral resolution is ~ 0.5 μm (using a data pixel density of 740×480 and a field of view of 165 μm×124 μm). The instrument is capable of resolving height differences of 0.1 nm. The heights h_{ij} (Fig. 2A) collected at all pixels are averaged over the entire field of view to provide an average surface height ($\bar{h}$) relative to a level datum. During dissolution, surface height is lost as the surface retreats, and thus changes in average height ($\Delta\bar{h}$) made at timed intervals (Δt) yield a retreat velocity:

$$\frac{\Delta\bar{h}}{\Delta t} = v_{[hk1]} \quad (1)$$

Dividing this velocity by the molar volume $\bar{V}$ gives a dissolution rate in the familiar units of moles per unit area per unit time:

$$r = v_{[hk1]}\bar{V}^{-1} \quad (2)$$

This approach allows a simple and straightforward calculation of surface area-specific rates from measurements of average surface heights ($\bar{h}$), and avoids the complexity of extracting rates from individual etch pit depths, in which additional data on etch pit density would be required. We also note that this rate measurement accomplishes in a single step the two separate measurements required to recover a rate from mineral powders (bulk solution composition and surface area determinations).

All experiments used cleavage rhombs prepared from the same high purity, synthetic calcite single crystal, the identical material used by Lea et al. (2001), obtained from Commercial Crystal Laboratories (Naples, Florida). Rhombs were cleaved with a razor blade and mounted immediately with a commercial epoxy resin to a fixed and oriented titanium holder. The mounted sample was placed inside a fluid flow cell (described below) and allowed to react under flow for a fixed time (Δt_1). The sample mount was then removed from the flow cell and mounted with constant orientation and position on the interferometer's stage. After *ex situ* VSI surface topography measurements ($\Delta_1\bar{h}$) were acquired, the sample mount was returned to the flow cell. The sample was then allowed to react under flow for the next time interval (Δt_2), and returned to the interferometer. Height data as a function of time were acquired by simply repeating this sequence. Measurements were made only over (initially) flat, smooth areas of the calcite cleavage surface, and the implications of this practice are discussed later. Re-

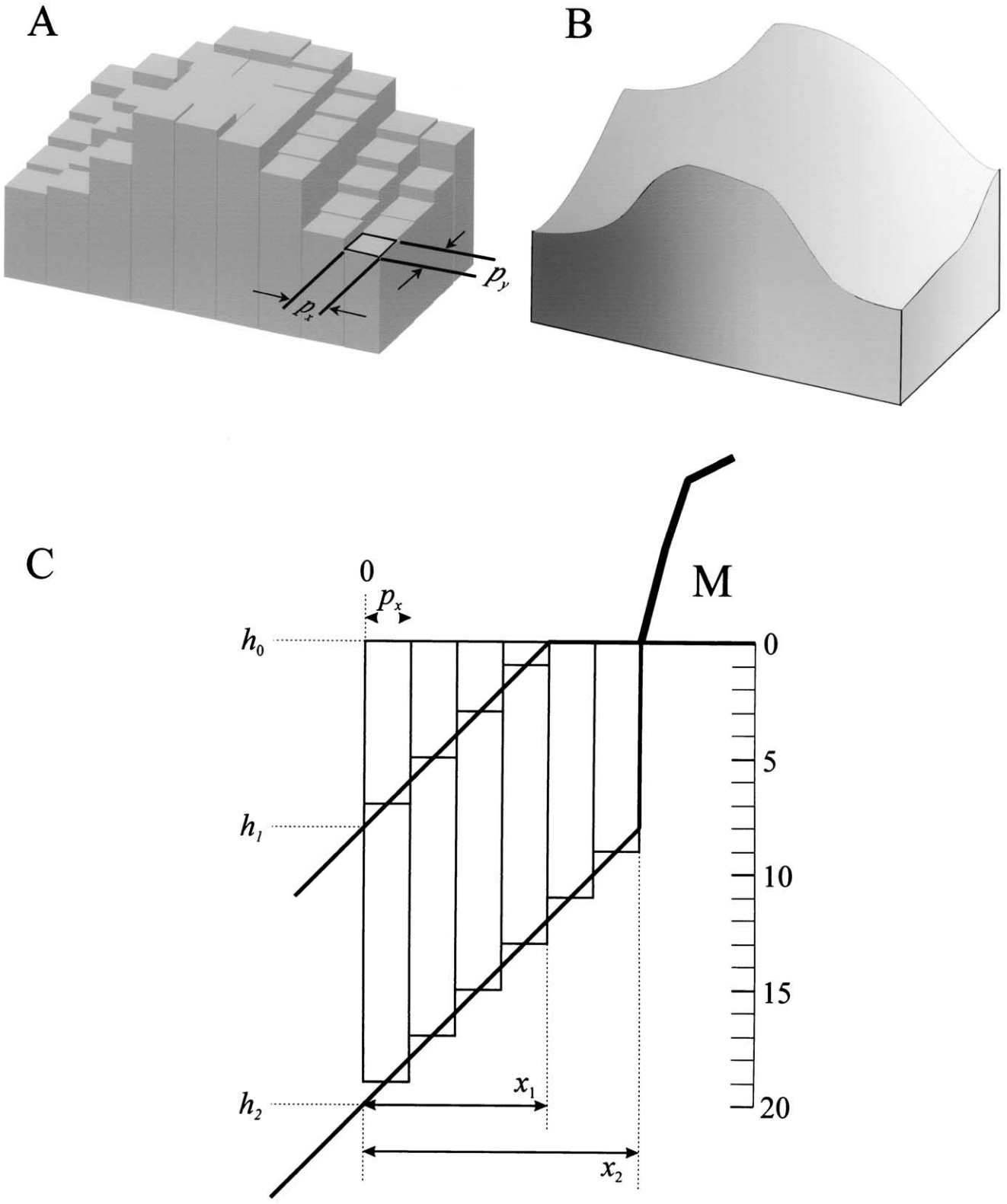

Fig. 2. Relationship of continuous mineral surface topography (B) to the discretized result (A) collected by the interferometer, limited by the single pixel area $p_x \times p_y$. (C) Simplified view of surface height changes at an etch pit wall, advancing to the right. Area below mask 'M' does not have access to solution. Heights h_0, h_1, and h_2 are depths of the surface at $x = 0$ at times t_0, t_1, and t_2, respectively, in arbitrary units ($h_1 = 8$, $h_2 = 20$). The purpose here is to illustrate that the sum of average heights, shown here in two dimensions for simplicity, is equivalent (within error) to the actual surface height. At time t_1, actual amount of mass removal = h_1 ($x_1/2$); measured interferometric result = (h_1 $x_1/4$) ($^7/_8$ + $^5/_8$ + $^3/_8$ + $^1/_8$) + ε_1 = h_1 ($x_1/2$) + ε_1, where ε_1 is the error imposed by the instrument's vertical and lateral resolution. As $h_1 = 0.4\ h_2$, at time t_2 actual height = ($h_1 + h_2$) $x_2/2 = 0.7\ h_2\ x_2$; measured height = ($h_2\ x_2/6$) ($^{19}/_{20}$ + $^{17}/_{20}$ + $^{15}/_{20}$ + $\cdots$ + $^9/_{20}$) + $\varepsilon_2 = 0.7\ h_2\ x_2 + \varepsilon_2$, etc. These relationships hold true despite the fact that etch pit walls are not smooth (as illustrated for simplicity), but composed of discrete steps and terraces.

duction of raw height data (i.e., $h \rightarrow \bar{h}$) also involved a leveling step in software (equivalent to hardware leveling of the microscope's stage). This step was accomplished by orienting flat areas interstitial to etch pits normal to the microscope's optic path (surface-normal height). There is a potential for introducing out-of-level height errors in this step; however, given the subnanometer vertical resolution of the instrument, we estimate the *maximum* error from out-of-level volume contributions to be 25%. The fact that rates are computed from *height differences* ($\Delta\bar{h}$) between sequential time steps also tends to minimize the accumulation of systematic errors. However, this approach worked best for surfaces that still included some smooth, relatively flat interstitial areas not directly impinged by etch pit growth. Because these interstitial areas have essentially been consumed by pit coalescence after approximately four hours of reaction, we restricted our rate calculations to surfaces reacted for less than four hours. However, layer-by-layer removal of material by accumulated lateral migrations of steps or stepwaves (originating at etch pits) across these interstitial areas will also generate net retreat of the surface *in addition to* that measured as height changes associated with etch pit development. This scenario is consistent with both the rate law of Lasaga and Luttge (2001) as well as numerous AFM observations. To measure this "background" rate (cf. v_b of MacInnis and Brantley 1992, their Table 2, p. 1121), we also conducted a separate experiment in which a removable (commercial silicone polymer) mask was applied to the surface to prevent solution access, and dissolution allowed to proceed. After more than four hours the mask was removed and the height difference between the masked and unmasked area measured. The *total* rate of removal is the sum of the "global" reduction of the entire surface (measured by the height difference at the margin of the masked region and hereafter termed the *global* rate; volume 'G' of Fig. 3B), and that associated with local etch pit development (volume 'E' of Fig. 3B). The total rate (=local + global rate, or $\frac{G + E}{\Delta t}$ from Fig. 3B) thus requires maintenance of a masked surface as a datum. All adhesives used to mask or attach samples were completely cured before experiment. Complete removal of the silicone masking was a simple process, and there was no evidence of any reaction between the mask and the mineral surface.

Our experimental conditions ($NaHCO_3$-Na_2CO_3 solutions from 18.2 MΩ-cm water, 4.4 meq/L, PCO_2 fixed at $10^{-3.41}$ atm, pH 8.8, 25°C) are essentially identical to that of fluid cell AFM work by Liang et al. (1996) and Lea et al. (2001). The experiments were simple in design: a single cleavage rhomb was confined in an acrylic cell (760 μL nominal volume) supplied with fluid by a syringe pump (55 μL/s). Cumulative run times ranged from 2 min to over 4 h. To evaluate the effect of an inhibitor, we also conducted additional runs in which dissolved Mn (as $MnCl_2$) was added to give total concentrations of 1.0, 1.5, and 2.0 μM.

Aside from logging comparisons of the input and output pH, we did not attempt to compute "bulk" rates from the composition of reacted solution exiting our fluid cell. Given the small area of solid exposed to solution and the brief residence time of fluid within the cell, we would expect the change in solution composition to be quite small (e.g., submicromolar in calcium), and thus difficult to measure with precision. No difference was observed between inflow and outflow pH. We would also anticipate that fluid chemistry might include contributions from grain boundaries, a complication we wished to explicitly avoid by interferometric measurement of surface-normal retreat velocities.

3. RESULTS

Dissolution in pure (Mn-free) solution is characterized by the development of etch pits. Isolated pits make their appearance almost immediately (within the first 10 min of reaction) as discrete, euhedral features, approximately 1 μm on a side, and are initially separated by relatively flat, interstitial terraces. Although some pits increase their volume primarily through deepening of the pit floor, many shallow etch pits grow also by lateral migration of the steps composing the pit walls (*cf. G1* and *G2* pits of MacInnis and Brantley 1992). This migration consumes interstitial areas, producing a complex surface of coalescent, intersecting pits. Characteristic surfaces having high etch pit density are shown as a series of time lapse topographic maps collected at steps of 1, 2, 3, and 4 h cumulative reaction in Figure 4A–D, and clearly illustrate the progressive expansion of etch pits over this 4 h time period. The outline of etch pits forming under these conditions do not form a true rhombic parallelogram. Instead, two adjacent sides fail to intersect at a distinct point, forming a curvilinear boundary (Fig. 3C–D). The floors of many of these pits are also not flat, but are deepest adjacent to this curved boundary. The crystallographic orientation of this rounding is constant and always involves the same pair of etch pit faces. In pure solution experiments, etch pits are also often organized as linear or curvilinear trench-like chains of closely spaced pits, whose total length may exceed several hundred microns. Coalescence renders these chains less recognizable as distinct features after 2 to 4 h reaction. The distribution of deep etch pits (i.e., depths on the order of 100 nm) is also very heterogeneous even on scales of hundreds of microns (e.g., Fig. 3A), and some areas of the surface show only isolated shallow (~1 nm deep) pits even after 4 h of dissolution.

The addition of dissolved Mn produces distinct changes in etch pit size, morphology, and distribution. After 7 min of reaction at concentrations of 1.0 μM Mn, etch pits are visible but lack the well-formed rhombic outline characteristic of pits observed in pure solution (i.e., in the absence of Mn) experiments (Fig. 5A). From 37 min of reaction onward (Fig. 5B–D), pit outlines progressively become more equant, and at 2 h resemble those seen in pure solution, but lack the curved boundary of adjacent sides (cf. Figs. 5D and 4B).

At 1.5 and 2.0 μM Mn (Fig. 5E–H) however, etch pits distributions are greatly reduced and large fractions of the mineral surface, i.e., entire fields of view under a 10× objective are essentially barren. Those few pits that are visible show irregular boundaries. The trench-like etch pit chains described above are absent. However, linear features that resemble abrasion scars or scoring traces do appear to become progressively enhanced with time, and are the most notable surface features. The origin of these features is not known, and may be present, although at the limits of resolution, even in pristine unreacted surfaces.

Figure 6A shows the reaction progress in terms of the decrease in average surface height as a function of time. Figure 6B shows the surface-normal retreat velocities computed from this slope ($\Delta\bar{h}/\Delta t$, Eqn. 1). Although rates were computed using surfaces that showed etch pit development, no attempt was made to account for lateral variation in etch pit distribution, and the error bars in Figure 6B reflect this variation. The mean dissolution rate over the interval of 1 to 3 h cumulative reaction time is $10^{-11.0}$ mols/cm^2/s (plotted also in Fig. 1). As explained previously, this value reflects the sum of the local etch pit rate and the global rate. Reaction rates are substantially depressed at Mn^{2+} concentrations greater than 1.0 μM (Fig. 6B–C). The rate at 1.0 μM is ~ 92% of the pure solution rate, whereas rates at 1.5 and 2.0 μM are 1 and 5% of the pure solution rate. The "global" rate was not measured separately in these inhibition experiments. These results are summarized in Table 1.

The inclusion of areas containing deep etch pit chains does not change the overall calculated rate. These chains are the

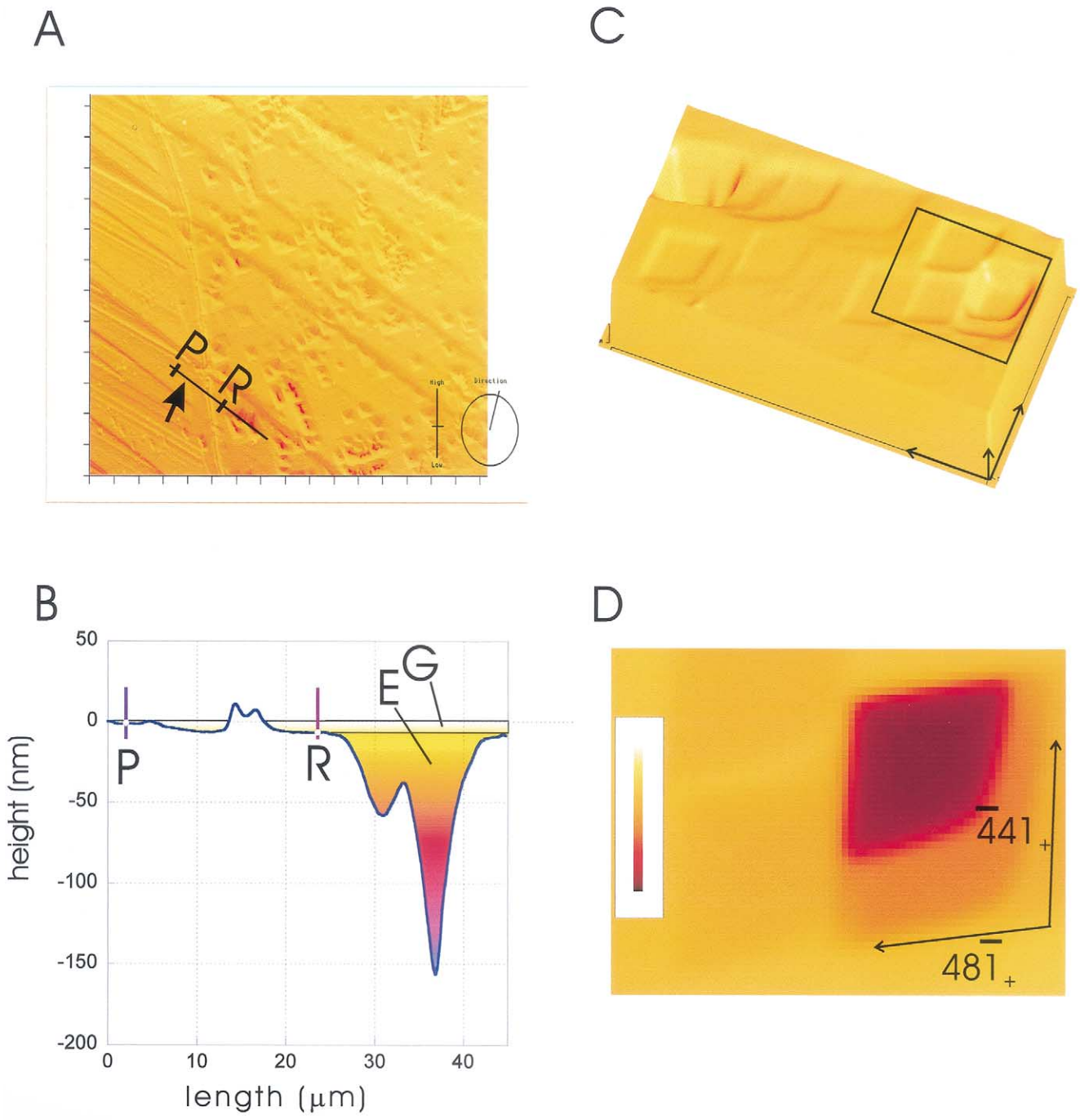

Fig. 3. Measurement of total calcite dissolution rate.

A. Relief map of calcite surface after 3 h reaction in pure solution. NW-SE profile line straddles the boundary (arrow) between pristine cleavage surface ('P') protected from reaction by inert adhesive mask, and the reacted surface ('R). Tick marks on image frame are spaced at 10 μm intervals.

B. Cross section profile from (A.) Total change in surface height is the sum of two components: a "global" elevation change ('G') and the change due to local growth of etch pits ('E'). Note large vertical exaggeration. Irregular elevation between ('P') and ('R') is artifact of adhesive mask. Boundary of 'G' and 'E' is parallel to original cleavage surface.

C. Three dimensional rendered surface showing shallow, coalescing etch pits with rounding of $[48\bar{1}]_+$ and $[\bar{4}41]_+$ steps. Scale bars: x, y = 10 μm; z = 100 nm.

D. Gradient map of inset from (C), showing coalescent etch pits. Color bar spans 88 nm.

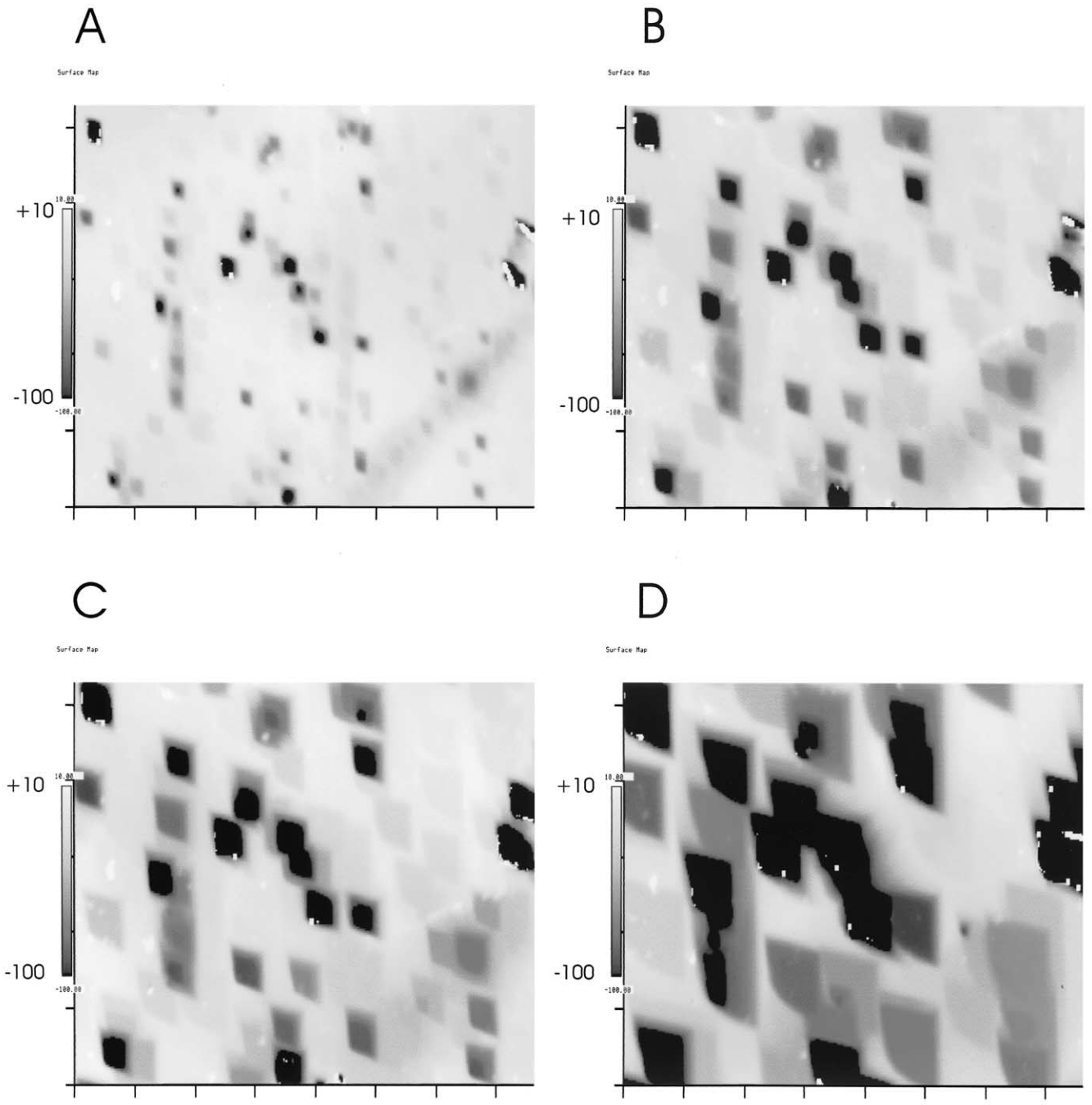

Fig. 4. Gradient topographic maps of a fixed area of calcite cleavage surface reacted for 1 (A), 2 (B), 3 (C), and 4 (D) elapsed hours. Surfaces are oriented so that $[48\bar{1}]_+$ and $[\bar{4}41]_+$ steps are migrating leftward and down, respectively. Note common orientation of etch pits, growth of pits by lateral expansion and deepening, and mutual interference and coalescence as reaction progresses. Vertical scale (color bar to left of each frame) is fixed at a total span of 110 nm to highlight surface detail, and thus deepest etch pit floors are off-scale; deepest pits are 373 nm (A), 561 nm (B), 609 nm (C), and 674 nm (D). Tick marks on image frame are spaced at 10 μm intervals.

deepest features in early time segments, and their overall contribution to average surface depth is of course greater than coexisting discrete, shallower pits. However, the inclusion or exclusion of these areas changed only the value of the intercept (in the context of a linear regression), and not the slope (i.e., the rate). Thus these chains seem to reflect defect features that persist only to shallow depth within the crystal, giving rise to rapid rates of early (i.e., within the first ~30 min) removal that then relax to coincide with the rate measured elsewhere. Although they are not visible immediately after cleaving, they may indicate damage incurred in this process.

Etch pits often occur in straight chains or linearly oriented

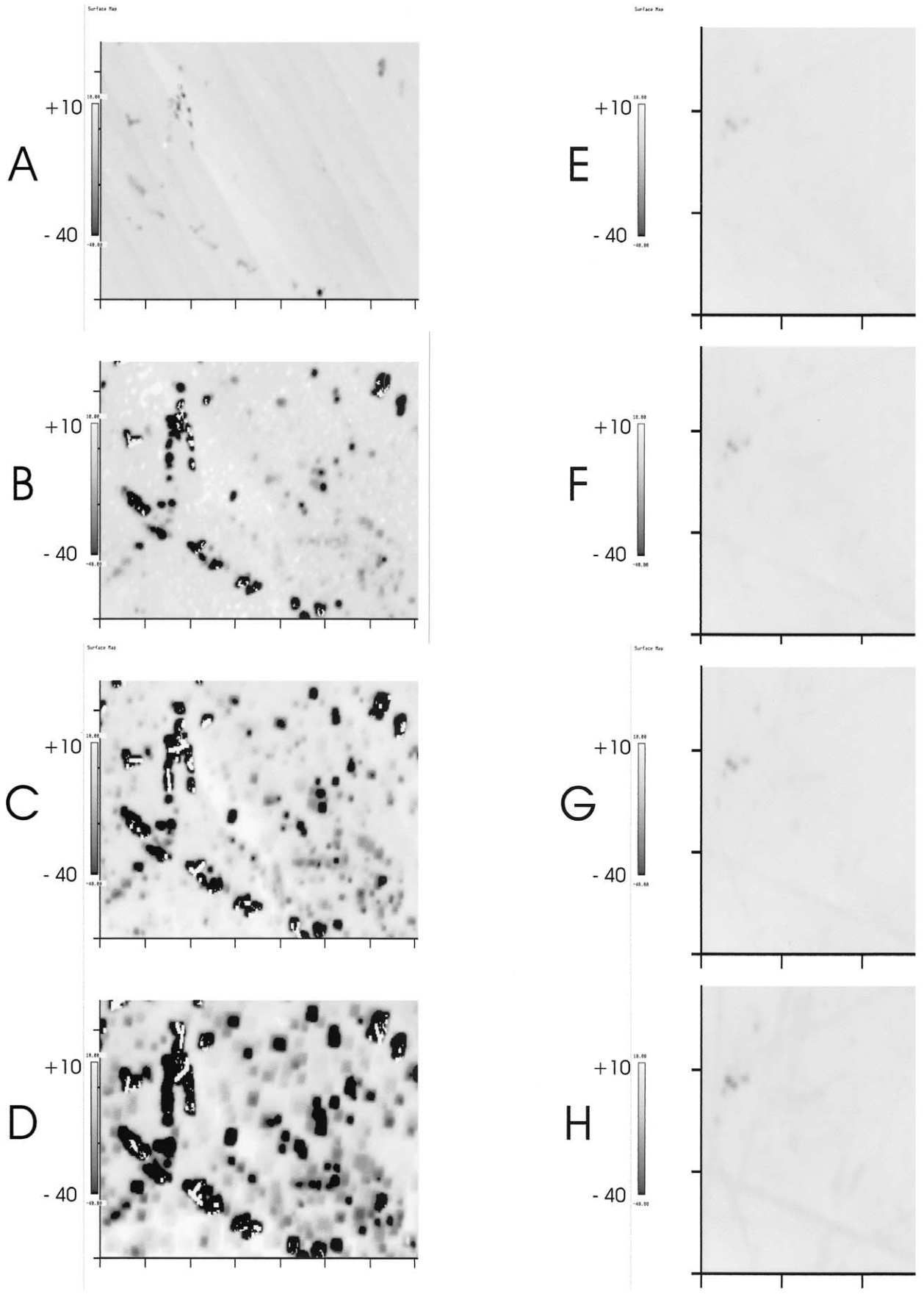

Fig. 5. Gradient topographic maps of a fixed area of calcite cleavage surface in solutions spiked with 1.0 μM (A-D) and 2.0 μM Mn^{2+} (E-H), collected at 7 min (A,E), 37 min (B,F), 1 h (C,G), and 2 (D,H) hours. Orientation with respect to $[48\bar{1}]_+$ and $[\bar{4}41]_+$ step directions is not known. The first pits to form in 1.0 μM Mn^{2+} are irregularly shaped and lack the rhombic outline observed in pure solution, but become relatively equant after 1 h of reaction, and lack a curved boundary. Etch pits are rare in 2.0 μM Mn^{2+} solutions, and show little change after 1 h. Color bars span 50 nm. Image frame ticks are spaced at 10 μm intervals.

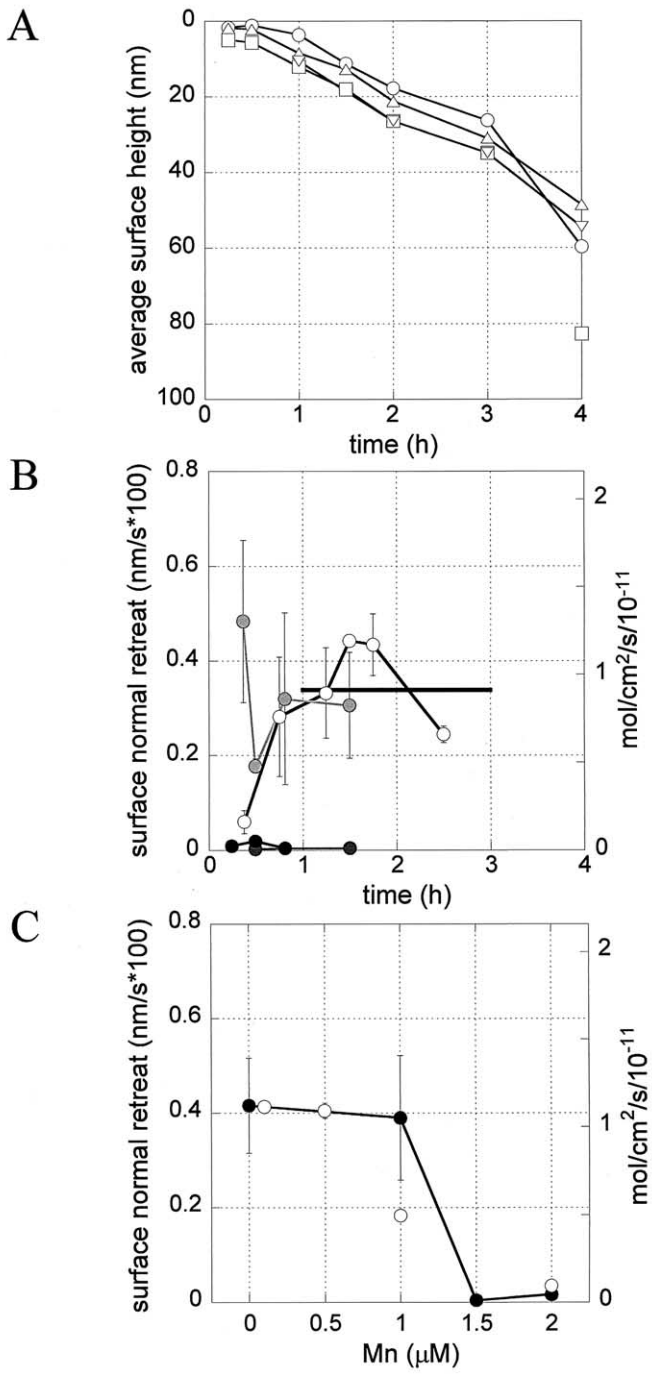

Fig. 6. Calcite dissolution rate measured by VSI.

A. Decrease in surface height (expressed here as depth) with elapsed reaction time in pure (Mn-free) solution. Slopes ($\Delta\bar{h}/\Delta t$) reflect surface-normal velocity. Early rates tend to be depressed relative to subsequent, steady state values. Symbols distinguish different surface data sets.

B. Computed dissolution rates expressed as surface normal retreat velocities (nm/s, left hand axis) and dissolution rates (mol/cm^2/s, right hand axis). Open circles = pure Mn-free solution; light gray, dark gray, and solid black filled circles = 1.0, 1.5 and 2.0 μM Mn^{2+} data, respectively. Horizontal line is mean for pure solution velocities. No correction is made for "global" retreat.

clusters, parallel to the $\langle 48\bar{1}\rangle$ or $\langle \bar{4}41\rangle$ direction. However, the origin of curvilinear pit chains of almost random orientation is not well understood. These features may reflect areas of concentrated but shallow strain introduced as an artifact during the act of preparing the cleavage surface itself. This is suggested by the fact that they eventually cannot be distinguished as surrounding single etch pits coalesce, and thus do not continue to serve as sites of preferred etch pit generation. Although they are the first pits to appear in pure solution experiments, they are also conspicuously absent in Mn^{+2}-added experiments.

4. DISCUSSION

4.1. Relationship of VSI Data to Powder Dissolution Dataset

The most important result of our study is the slow dissolution rate ($10^{-11.0}$ mols/cm^2/s) compared to rates derived from solution chemistry using either mineral powders (Plummer et al., 1978; Sjöberg 1978; Chou et al., 1989) or single crystals (Rickard and Sjöberg 1983; Schott et al., 1989; MacInnis and Brantley 1992). The differences between the VSI-measured rate and rates collected under similar conditions are summarized in Table 1 and in Figure 1, and range from a factor of ~ 5 to over 100. There are several potential sources of variability in measured rates of dissolution far from equilibrium in this alkaline region: back reactions involving dissolution products, grain size, and the distribution of reactive surface sites. The likelihood of these controls and the overall significance of these rate differences are discussed below.

At and above a critical flow rate (2.5 μL/s, 20 μL cell volume, τ = 8 s), Liang and Baer (1997, their Fig. 1, p. 277) showed step velocities to be independent of fluid flow. Concerns over differences in fluid cell design between our work and that of Liang and Baer (1997) prompted us to rerun experiments under identical solution conditions, but with reduced cell volumes and increased flow rates. These adjustments were sufficient to reduce residence times from τ = 14 to 4 s, one half that prevailing in Liang and Baer (1997). These data are not included here as they are part of a future paper, but we can report that we saw no difference in dissolution rate within the error of the measurement. We thus conclude that diffusive transport, and thus back reactions, are not limiting under the conditions of our experiments.

Many of the literature data reproduced in Figure 1 were conducted at a $PCO_2 \sim 0$, whereas our experiments used a fixed PCO_2 of $10^{-3.41}$ atm. At a given pH, an increase in PCO_2 demands an increase in dissolved carbon, and thus our rates were measured at a greater carbonate ion concentration than those taken from the literature. Consideration of the potential back reaction suggests that this should have the effect of reducing the rate. Lea et al. (2001) observed more than a ~50% decrease in step edge velocities as carbonate ion concentration was increased from ~0 to 150 μM; an increase to 900 μM

C. Comparison of AFM step velocities and VSI dissolution rates (including correction for "global" retreat) in Mn^{2+}-spiked solutions. Agreement between the VSI (closed circles) and AFM pure solution data (open circles, taken from Lea et al., 2001) requires a step density of ~ 9 steps μm^{-1} (assumed to be independent of Mn^{+2} inhibition).

Table 1. Experimental results of calcite dissolution rates measured by vertical scanning interferometry (50× Mirau objective), Pco_2 $10^{-3.41}$ atm, pH 8.82, 25°C.

Conditions	Total analytical area (μm^2)	pH	Surface-normal velocity (nm/s × 100)	log rate mol/cm^2/s
pure solution (Mn = 0)				
etch pit domains	11885	8.83	0.337 ± 0.101	−11.04
"global" surface retreat		8.83	0.078 ± 0.020	−11.68
total rate		8.83	0.415 ± 0.120	−10.95
Mn^{+2}–doped				
Mn = 1.0 μM	17730	8.82	0.311 ± 0.131	−11.08
Mn = 1.5 μM	3812	8.82	0.003 ± 0.001	−13.04
Mn = 2.0 μM	6296	8.82	0.016 ± 0.009	−12.36

brought about a further ~50% reduction. Busenberg and Plummer (1986) described the role of carbonate ion through a dehydration back reaction. In experiments far from equilibrium at pH 9.8 and a wide range of total dissolved carbon concentrations (Table 6, p. 154, Busenberg and Plummer 1986), their measured rate progressively decreases as total carbon (and thus carbonate ion) concentrations increase, reaching a minimum of $10^{-10.61}$ moles/cm^2/s at 0.3 mol/L total carbon (and a computed CO_3^{2-} molality of 0.14). However, at the carbonate ion concentrations of our experiments, their published rate is between $10^{-10.07}$ and $10^{-10.26}$ (CO_3^{2-} concentrations of 150 and 250 μmol/kg-H_2O, respectively), i.e., still between ~5 to 7 times faster than our measured rate.

Another potential factor affecting experimental dissolution rates is grain size. A decrease in grain size below a critical diameter will increase the solubility and distance from equilibrium, and thus the driving force for dissolution. However, the point at which particle size makes a significant contribution to total free energy has been estimated at ~0.1 μm for calcite (Morse and Wang 1996). Thus given the magnitude of grain sizes reported in powder experiments in Table 1, it is unlikely that this effect *alone* is a factor in the variability of dissolution rates observed here. Interferometer-derived rates are independent of particle size altogether, as these are measured by surface retreat of a large, single crystal. It is also conceivable that rate variations within the powder dataset reflect variability in trace impurities or contaminants (e.g., phosphate), contributed either from reagents, analytical methods, or from the dissolving solid itself (e.g., Morse 1974; Sjöberg 1978; Plummer et al., 1979; Eisenlohr et al., 1999). These factors are of even greater importance in single crystal measurements because of the limited reactive area.

However, grain size may still play a role in measured dissolution rates of mineral powders. It has been suggested (e.g., Dove and Platt 1996) that the discrepancy in rates measured from AFM versus bulk powder reactors reflects the relationship of step density and reactivity. Figure 7 shows the details of a grain in which step and kink densities increase at edges and corners relative to the smooth terraces characterizing the faces. If step and kink density are higher (i.e., smaller step and kink *spacing*), a step velocity identical to that limiting dissolution on smooth terraces will produce a higher bulk rate. The rate contribution from these areas of high step and kink density may also be higher than their contribution to total surface area, and thus the normalization with respect to surface area will still yield a rate higher than that measured elsewhere (e.g., at flat terraces). In the context of the rate law introduced by Lasaga and Luttge (2001), grain edges may thus yield a more efficient means of generating steps. In addition, stepped and kinked surfaces at grain edges and corners would also make a greater contribution to total surface area as grain diameter decreased, increasing bulk reactivity further. The interferometer, in contrast, measures the result of largely etch pit-controlled (at least

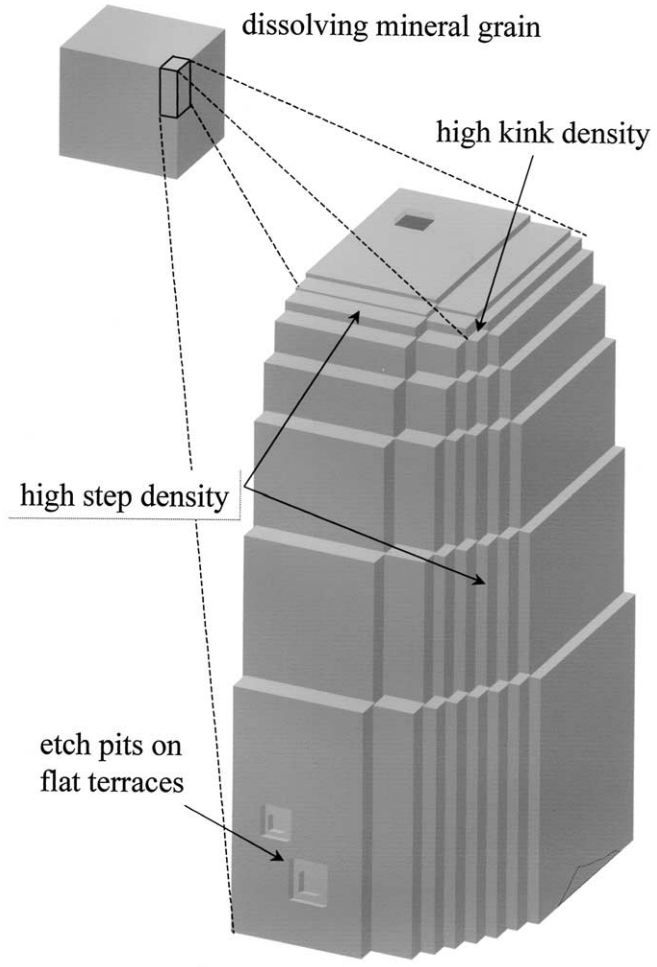

Fig. 7. Distribution of step and kink distribution on mineral particles, showing higher (cleavage) step and kink densities at edges and corners versus flat terraces.

in the case of calcite) step retreat on flat terraces. Step densities are also higher at etch pits, but the distribution and spacing of steps surrounding etch pits reflects their generation by the pit itself and the velocity distribution around a dislocation core (Lasaga and Luttge 2001).

The question of whether our rates represent steady state behavior does not have a simple answer. Because etch pit development is such a large component of the overall rate, variations in etch pit (i.e., defect) distribution are the probable source of the apparent error ($\sim$ 30% in pure solution runs) in our rates (Fig. 6B). These variations do not reflect experimental errors in height measurement, which, given the instrument's high resolution and reproducibility, are much smaller. As older etch pits widen and coalesce, new etch pits often nucleate in existing pit floors (Figs. 3C–D and 4), a phenomenon discussed in detail by MacInnis and Brantley (1992). They determined calcite dissolution rates both by normalizing changes in fluid composition (pH) to the surface area painstakingly derived by photomicrography (using a differential interference objective for *x–y* and Mirau double beam interference objective for *z*), and by calculating the volume removed by etch pits. They concluded that maintenance of a steady state consistent with the rate (3.1×10^{-10} mol/cm^2/s, cleaved unstrained calcite) and etch pit distributions observed in their experiments demands discontinuous nucleation of pits at dislocations. We cannot evaluate this assertion based on our data alone, nor can we offer an explanation as to why our rate is more than an order of magnitude lower. However, our data do suggest that a steady state rate may be a fortuitous occurrence. Although the volume increase of, for example, a single deep pit may be linear with respect to time (at least over 4 h of observation), this growth rate will obviously not persist indefinitely. Once the pit reaches the dislocation's terminus, further deepening would require the random nucleation of a local hole to generate step waves, an event that Lasaga and Luttge (2001) have demonstrated is unlikely even far from equilibrium. As the total rate measured on calcite cleavage surfaces reflects the sum of defect (etch pit) controlled excavation and the much slower, "global" rate, a constant total rate having a statistical variation less than what we have observed here would also require a constant dislocation density. Our data suggest that this is a requirement not easily satisfied.

4.2. The Effect of Mn Addition and Relationship to AFM Rates

Previous experimental studies have amply demonstrated inhibition of calcite dissolution rate by dissolved manganese and other metal cations (Terjesen et al., 1961; Nestaas and Terjesen 1969; Gutjahr et al., 1996). Salem et al. (1994) also measured large reductions in dissolution rate with the addition of Mn^{+2} at micromolar to submicromolar concentrations (pH 9.2, $CaCl_2$-$NaHCO_3$ solutions). These reductions were interpreted as reversible Langmuir-type adsorption reactions at specific surface sites. Lea et al. (2001) also record significant inhibition by Mn^{+2}, in the form of reduced step velocities with addition of greater than 0.5 μM Mn^{+2}; we compare our rate data with these results in the subsequent discussion.

All etch pits formed in pure solution runs showed rounding at one corner, identified by Liang et al. (1996) and Lea et al. (2001) as the intersection of the $[48\bar{1}]_+$ and $[\bar{4}41]_+$ steps, although the opposing $[48\bar{1}]_-\hat{}[\bar{4}41]_-$ corner remains sharp (e.g., Fig. 3C–D). With increasing Mn^{+2} concentration, we observed that interfacial aspects of etch pits became substantially less distinct, with apparent rounding affecting all step faces. It is clear that Mn^{2+} addition brings about a decrease in etch pit nucleation. We did not measure a "global" rate in the Mn experiments, although we expect that this rate may also be reduced proportionally. Surfaces reacted with 1.5 and 2.0 μM Mn^{2+} revealed many areas to be entirely free of etch pit development within the field of view, even after several hours of reaction. Thus the rates presented in Table 1, associated with areas of locally high etch pit density, may reflect maximum values. Assuming that these results do not reflect variations in defect density among various cleavage samples, it appears that beyond a critical concentration of inhibitor ion, etch pits (at least those large enough to be visible to the interferometer) fail to nucleate on a large scale. Those few that do manage to nucleate are severely deformed, lack rhombic shape and show walls that are convex towards the pit center of the walls, possibly reflecting an asymmetric pattern of reduction in step velocities dependent on step geometry. In addition, Mn^{2+} concentrations of 1.5 $\sim$ 2 μM at this pH and alkalinity yield slight supersaturations with respect to $MnCO_3$. For example, EQ3NR (Wolery 1992) computes log $\Omega_{MnCO3} \sim 0.2$ at 2 μM Mn^{2+}. In comparison, Lea et al. (2001) have shown that at Mn^{2+} concentrations of 2 μM, a lath-shaped epitaxial phase nucleates on the surface along the $\langle 2\bar{2}1\rangle$ direction. Once nucleated, the phase continues to grow, even at lower Mn^{2+} concentrations, and likely is a Ca-Mn carbonate solid solution (Lea et al., 2003). Thus, it is possible that the reduction in rate results from initial adsorption of Mn^{2+} and ultimate precipitation of a thin (Mn, Ca)CO_3 layer at critical reaction sites.

Recent SFM/AFM work on calcite has focused on step velocities, particularly in the vicinity of etch pits (e.g., Hillner et al., 1992a, 1992b; Gratz et al., 1993; Stipp et al., 1994; Dove and Platt 1996; Liang et al., 1996; Britt and Hlady 1997; Liang and Baer 1997; Jordan and Rammensee 1998; Davis et al., 2000; Teng et al., 2000; Lea et al., 2001). A comparison of AFM step velocities to VSI surface-normal velocities (and thus to bulk powder rates) requires a value for step height and step density. Although this latter term is not often measured, the previous discussion has already enunciated its importance. As mentioned previously, we have intentionally maintained experimental conditions identical to those of Lea et al. (2001). We have thus recalculated their step velocity data, assuming a step height of 0.3 nm, and have incorporated a step density sufficient to produce a surface-normal rate that is a close match to our dataset.

This comparison is shown in Figure 6C. A match of the pure solution VSI and AFM data requires an approximate step density of $\sim$ 9 μm^{-1} (equivalent to a step spacing of 113 nm). This computed step density is close to the minimum observed by Jordan and Rammensee (1998; $\sim$ 5 μm^{-1} for fast steps, $\sim$ 15 for slow steps, their Fig. 2, p. 943; see also Table 1). The fact that a coincidence between AFM step velocities and our surface-normal retreat velocity demands a low step density is consistent with the stepwave model of Lasaga and Luttge (2001), which predicts that the spacing of steps should reach a maximum steady state value as they propagate away from etch pit centers.

However, a step density consistent with the slow "global" rate we observed would be lower still: less than $\sim 2\ \mu m^{-1}$.

5. CONCLUSIONS

The dissolution rate of a calcite cleavage surface measured by vertical scanning interferometry at a pH close to 9 and a fixed PCO_2 of $10^{-3.41}$ atm is $10^{-11.0}$ mol/cm^2/s at room temperature. Rates are determined by measuring the change in mean surface height as a function of time. Dissolution occurs through deepening of etch pits, the lateral migration of etch pit walls, and an overall "global" removal of material in areas outside major etch pit domains. The most noteworthy observation is that the VSI rate is slower than rates reported in powder and other single crystal experiments by more than one order of magnitude, although agreement between VSI and computed AFM rates in certain cases is quite close. Introduction of Mn^{2+} at concentrations greater than 1.0 μM results in a large decrease in etch pit density and associated dissolution rate, and distorts etch pit geometry.

We do not completely understand the significance of the poor agreement with powder rates. However, we suggest that the differences may lie in the fact that interferometry measures a surface-normal dissolution rate without contributions from grain edge boundaries having high step and kink density. These contributions to the bulk rate would be amplified as grain size decreases. In similar interferometer measurements of dolomite dissolution rate at pH 3, Luttge et al. (2003) also obtained rates that are several times slower than those returned by powders. We also observed great variation with respect to the overall distribution of etch pits. Our measurements focused on areas in which (initial) etch pit density was approximately constant. However, we also noted areas that were essentially barren in terms of etch pit development. The rate in these etch pit-poor domains would be limited by the global rate (Table 1). The fact that the "global" rate is a relatively minor contribution to the total rate implies potentially large variations in reactivity even in terrace areas.

Acknowledgments—We thank A. Scott Lea for the calcite crystals and helpful discussions. The manuscript was substantially improved by an insightful analysis provided by Professor Susan L. Brantley, as well as the comments of two anonymous reviewers and the Associate Editor. RSA also thanks Professor John Morse (Texas A&M University), as well as Mikala Beig and Kevin Davis (Rice University) for many discussions concerning mineral surface kinetics. This work was supported in part by the Office of Basic Energy Science, Geosciences Research Program, U.S. Department of Energy, and by subcontract from Battelle/PNNL to Rice University (400635A9E). AL acknowledges support from Rice University (D71602) as well as NSF (EAR0125667). Pacific Northwest National Laboratory is a multiprogram national laboratory operated by Battelle Memorial Institute for the U.S. Department of Energy under Contract DE-AC06 to 76RL0 1830.

Associate editor: A. Mucci

REFERENCES

Beig M., Arvidson R. S., and Luttge A. (2002) A new experimental method for direct comparison of single-crystal and powder dissolution rates. The Geological Society of America 2002 Annual Meeting (Denver, October 27–30, 2002), Abstracts with Programs **34**(b), 418.

Blum A. E. and Lasaga A. C. (1987) Monte Carlo simulations of surface reaction rate laws. In: *Aquatic Surface Chemistry, Chemical Processes at the Particle-water Interface* (ed. W. Stumm), pp. 255–292. Wiley, New York.

Brantley S. L., Crane S. R., Crerar D. A., Hellmann R., and Stallard R. (1986) Dissolution at dislocation etch pits in quartz. *Geochim. Cosmochim. Acta* **50,** 2349–2361.

Brantley S. L., White A. F., and Hodson M. E. (1999) Surface area of primary silicate minerals. In: *Growth, Dissolution and Pattern Formation in Geosystems* (eds. B. Jamtveit and P. Meakin), pp. 291–326. Kluwer Academic Publishers, Dordrecht.

Brantley S. L. and Mellott N. P. (2000) Surface area and porosity of primary silicate minerals. *Am. Mineral.* **85,** 1767–1783.

Britt D. W. and Hlady V. (1997) *In-situ* atomic force microscope imaging of calcite etch morphology change in undersaturated and 1-hydroxyethylidene-1,1-diphosphonic acid poisoned solutions. *Langmuir* **13,** 1873–1876.

Busenberg E. and Plummer L. N. (1982) The kinetics of dissolution of dolomite in CO_2-H_2O systems at 1.5 to 65°C and 0 to 1 Atm PCO_2. *Amer. J. Sci.* **282,** 45–78.

Busenberg E., Plummer L. N. (1986) A comparative study of the dissolution and precipitation kinetics of calcite and aragonite. In *Studies in Diagenesis*. (ed. F. A. Mumpton), pp. 139–168. U.S. Geological Survey Bulletin.

Chou L., Garrels R. M., and Wollast R. (1989) Comparative study of the kinetics and mechanisms of dissolution of carbonate minerals. *Chem. Geol.* **78,** 269–282.

Davis K. J., Dove P. M., and De Yoreo J. J. (2000) The role of Mg^{2+} as an impurity in calcite growth. *Science* **290,** 1134–1137.

Dove P. M. and Platt F. M. (1996) Compatible real-time reaction rates for in situ imaging of mineral-water interactions using scanning force microscopy. *Chem. Geol.* **127,** 331–338.

Eisenlohr L., Meteva K., Grabrovšek F., and Dreybodt W. (1999) The inhibiting action of intrinsic impurities in natural calcium carbonate minerals to their dissolution kinetics in aqueous H_2O-CO_2 solutions. *Geochim. Cosmochim. Acta* **63,** 989–1002.

Gautier J.-M., Oelkers E. H., and Schott J. (2001) Are quartz dissolution rates proportional to B.E.T. surface areas? *Geochim. Cosmochim. Acta* **65,** 1059–1070.

Gratz A. J., Hillner P. E., and Hasma P. K. (1993) Step dynamics and spiral growth on calcite. *Geochim. Cosmochim. Acta* **57,** 491–495.

Gutjahr A., Dabringhaus H., and Lacmann R. (1996) Studies of the growth and dissolution kinetics of the $CaCO_3$ polymorphs calcite and aragonite II. The influence of divalent cation additives on the growth and dissolution rates. *J. Cryst. Growth* **158,** 310–315.

Hillner P. E., Manne S., Gratz A. J., and Hasma P. K. (1992a) AFM images of dissolution and growth on a calcite crystal. *Ultramicros.* **42–44,** 1387–1393.

Hillner P. E., Gratz A. J., Manne S., and Hasma P. K. (1992b) Atomic-scale imaging of calcite growth and dissolution in real time. *Geol. (Bould.).* **20,** 359–362.

Jordan G. and Rammensee W. (1998) Dissolution rates of calcite $(10\bar{1}4)$ obtained by scanning force microscopy: Microtopography-based dissolution kinetics on surface with anisotropic step velocities. *Geochim. Cosmochim. Acta* **62,** 941–947.

Lasaga A. C. and Luttge A. (2001) Variation of crystal dissolution rate based on a dissolution stepwave model. *Science* **291,** 2400–2404.

Lea A. S., Amonette J. E., Baer D. R., Liang Y., and Colton N. G. (2001) Microscopic effects of carbonate, manganese, and strontium ions on calcite dissolution. *Geochim. Cosmochim. Acta* **65,** 369–379.

Lea A. S., Hurt T. T., El-Azab A., Amonette J. E., and Baer D. R. (2003). Heteroepitaxial growth of a manganese carbonate secondary nano-phase on the $(10\bar{1}4)$ surface of calcite in solution. *Surf. Sci.* (in press).

Liang Y., Baer D. R., McCoy J. M., Amonette J. E., and LaFemina J. P. (1996) Dissolution kinetics at the calcite-water interface. *Geochim. Cosmochim. Acta* **60,** 4883–4887.

Liang Y. and Baer D. R. (1997) Anisotropic dissolution at the CaCO3 $(10\bar{1}4)$-water interface. *Surf. Sci.* **373,** 275–287.

Luttge A., Bolton E. W., and Lasaga A. C. (1999) An interferometric study of the dissolution kinetics of anorthite: the role of reactive surface area. *Am. J. Sci.* **299,** 652–678.

Luttge A., Winkler U., Lasaga A. C. (2002) An interferometric study of the dolomite dissolution: A new conceptual model for mineral dissolution. *Geochim. Cosmochim. Acta* in press.

MacInnis I. N. and Brantley S. L. (1992) The role of dislocations and surface morphology in calcite dissolution. *Geochim. Cosmochim. Acta* **56,** 1113–1126.

Morse J. W. (1974) Dissolution kinetics of calcium carbonate in sea water. III: A new method for the study of carbonate reaction kinetics. *Am. J. Sci.* **274,** 97–107.

Morse J. W. (1983) The kinetics of calcium carbonate dissolution and precipitation. In: *Carbonates: Mineralogy and Chemistry, Reviews in Mineralogy*, (ed. R. J. Reeder), vol. 11, pp. 227–264. Mineralogical Society of America, Washington, DC.

Morse J. W. and Arvidson R. S. (2002) The dissolution kinetics of major sedimentary carbonate minerals. *Earth Sci. Rev.* **58,** 51–84.

Morse J. W. and Wang Q. (1996) Factors influencing the grain size distribution of authigenic minerals. *Am. J. Sci.* **296,** 989–1003.

Nestaas I. and Terjesen S. G. (1969) The inhibiting effect of scandium ions upon the dissolution of calcium carbonate. *Acta Chemica Scandinavica* **23,** 2519–2531.

Plummer L. N., Wigley T. M. L., and Parkhurst D. L. (1978) The kinetics of calcite dissolution in CO_2-water systems at 5° and 60°C and 0.0 to 1.0 atm CO_2. *Am. J. Sci.* **278,** 179–216.

Plummer L. N., Parkhurst D. L., and Wigley T. M. L. (1979) Critical review of the kinetics of calcite dissolution and precipitation. In: *Chemical Modeling—Speciation, Sorption, Solubility and Kinetics in Aqueous Systems* (ed. E. Jenne), pp. 537–573. American Chemical Society, Washington, D. C.

Rickard D. T. and Sjöberg E. L. (1983) Mixed kinetic control of calcite dissolution rates. *Am. J. Sci.* **283,** 815–830.

Salem M. R., Mangood A. H., and Hamdona S. K. (1994) Dissolution of calcite crystals in the presence of some metal ions. *J. Mat. Sci.* **29,** 6463–6467.

Schott J., Brantley S., Crerar D., Guy C., Borcsik M., and Williame C. (1989) Dissolution kinetics of strained calcite. *Geochim. Cosmochim. Acta* **53,** 373–382.

Shiraki R., Rock P., and Casey W. H. (2000) Dissolution kinetics of calcite in 0.1 M NaCl solution at room temperature: An atomic force microscopic (AFM) study. *Aqua. Geochem.* **6,** 87–108.

Sjöberg E. L. (1976) A fundamental equation for calcite dissolution kinetics. *Geochim. Cosmochim. Acta* **40,** 441–447.

Sjöberg E. L. (1978) Kinetics and mechanism of calcite dissolution in aqueous solutions at low temperatures. *Stockholm Contrib. Geol.* **32,** 92.

Sjöberg E. L. and Rickard D. T. (1983) The influence of experimental design on the rate of calcite dissolution. *Geochim. Cosmochim. Acta* **47,** 2281–2285.

Stipp S. L. S., Eggleston C. M., and Nielsen B. S. (1994) Calcite surface structure observed at microtopographic and molecular scales with atomic force microscopy (AFM). *Geochim. Cosmochim. Acta* **58,** 3023–3033.

Teng H. H., Dove P. M., Orme C. A., and De Yoreo J. D. (2000) Thermodynamics of calcite growth: baseline for understanding biomineral formation. *Science* **282,** 724–727.

Terjesen S. G., Erga O., Thorsen G., and Ve A. (1961) II. Phase boundary processes as rate determining steps in the reaction between solids and liquids. The inhibitory action of metal ions on the formation calcium bicarbonate by the reaction of calcite with aqueous carbon dioxide. *Chem. Eng. Sci.* **74,** 277–288.

Wolery T. J. (1992) EQ3NR, A Computer Program for Geochemical Aqueous Speciation-Solubility Calculations. (Version 7.0): UCRL-MA-110662-PT-I, Lawrence Livermore National Laboratory, Livermore, California.